RSC Advances

ROYAL SOCIETY OF CHEMISTRY

www.rsc.org/advances

A table of contents entry.

Colour graphic:	Text:
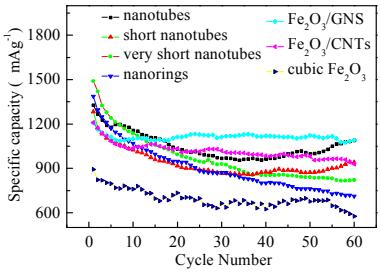	The cycling performance of hollow structure α-Fe_2O_3 improves with the increase of aspect rations.

Synthesis and the Comparative Lithium Storage Properties of Hematite: Hollow Structures vs. Carbon Composites

Chao Wu [a,b], Quan-Chao Zhuang [a,*], Lei-Lei Tian [a], Yong-Xin Wu [c], Zhi-Cheng Ju [a], Hong Zhang [a], Xin-Xi Zhang [d], Hong-Bo Chen [b]

[a] Li-ion Batteries Lab, School of Materials Science and Engineering, China University of Mining & Technology, Xuzhou 221116, China; [b] Xuzhou Mining Group Corporation, Xuzhou 221006, China; [c] Bozhou Teachers College, Bozhou 236800, China; [d] School of Chemical Engineering and Technology, China University of Mining & Technology, Xuzhou 221116, China;

Abstract: In the present work, the α-Fe_2O_3 hollow structures from nanotubes to nanorings, and α-Fe_2O_3/carbon composites composed of nanoparticles homogeneously dispersed on graphene sheets and carbon nanotubes were synthesized via a self-assemble combined with a facile hydrothermal method, respectively, and its structure, morphology and electrochemical performance were characterized by XRD, XPS, SEM, TEM, CV, charge-discharge test and EIS. The focus is put on elucidating how structural aspects, such as particle size and shape of nanoparticles as well as carbon matrix, influence the electrochemical properties of the α-Fe_2O_3 nanoparticles. The results revealed that the cycling performance of hollow structure α-Fe_2O_3 improves with the increase of aspect rations, namely, the α-Fe_2O_3 nanotubes exhibit the best electrochemical performance in terms of reversible capacity, capacity retention and rate performance, which is comparable to that of α-Fe_2O_3

* To whom correspondence should be addressed. Tel: +86 516 83591877 and Fax: +86 516 83591870. E-mail address: zhuangquanchao@126.com.

nanoparticles-carbon composites. It is expected that the synthesis of α-Fe_2O_3 naonotubes with high aspect rations anchored on conducting graphene would be potential anode materials for high performance LIBs.

Keywords: α-Fe_2O_3; Nanotubes; Composites; Anode; Lithium-ion batteries

1 Introduction

Lithium-ion batteries (LIBs) are important power sources for portable electronic devices. In addition, LIBs are also growing in popularity for electric vehicles, military, and stationary power grid storage. So as to meet the ever-growing demand for high energy density and high power, it is essential to develop novel electrode materials with high-performance for next generation LIBs. Correspondingly, transition metal oxides have been paid a lot of attention as LIBs anodes, because they have much higher theoretical capacities than the current commercial anode material (graphitic materials). Since transition metal oxides undergo conversion reaction $2yLi^+ + 2ye^- + Me_xO_y \rightarrow xMe + yLi_2O$, involving more than one Li ion per formula unit, exceptionally high specific capacities can be attained during the redox cycle [1-6]. Among the transition metal oxides, α-Fe_2O_3 (hematite) has been suggested as a promising candidate for replacing graphite due to its high theoretical capacity (1007 mAh g^{-1}), nearly three times larger than that of graphite (372 mAh g^{-1}), which has been widely investigated as the anode material for LIBs [6-10]. However, its large volume changes and severe particle aggregation associated with the cycling of Li^+ insertion/desertion process lead to electrode pulverization and loss of interparticle contact, thus resulting in a large irreversible capacity loss and a poor electrical conductivity. To

circumvent these obstacles, various attempts have been applied to these problems, which include (*i*) preparing the materials with hollow structures [11,12], (*ii*) embedding the materials in carbon matrix [13,14,15].

The hollow structural materials have many merits, which include (*i*) the large surface area endows the hollow materials with more lithium storage sites and a large electrode/electrolyte contact area for high Li^+ flux across the interface, (*ii*) the thin shells of permeable hollow materials could shorten the transport paths for both Li^+ ions and electrons, leading to good rate capacity, and (*iii*) the hollow structures with volume interior could be useful to alleviate the structural strain and accommodating the large volume variation associated with repeated Li^+ ions insertion/extraction processed, giving rise to improved cycling stability [6,7,16]. Moreover, carbon materials, which form a variety of allotropes, are commonly used matrixs, because of their good ion/electron conductivity, low volume expansion, and tolerance to mechanical stress, which not only buffers the volume changes but also refrains the aggregation of nanoparticles, therefore contributing to enhanced electrochemical performance [11,12,17,18].

In our previous studies [19-21], Fe@Fe_2O_3 core-shell nanoparticles attached to carbon nanotubes and α-Fe_2O_3 nanoparticles or Fe@Fe_2O_3 core-shell nanoparticles anchored on graphene hybrid materials were synthesized by using a hydrothermal reaction followed by an in situ thermal reduction. Its cycling performance and rate capability are drastically improved, highlighting the importance of the embedding nanoparticles in carbon matrix for maximum use of electrochemically active Fe_2O_3 nanoparticles and carbon nanomaterials for energy storage applications.

Herein, the cubic α-Fe_2O_3, α-Fe_2O_3 hollow structures (from nanotubes to nanorings) and α-Fe_2O_3/carbon (GNS or CNTs) composites composed of α-Fe_2O_3 nanoparticles homogeneously dispersed on GNS and CNTs were synthesized via a self-assemble combined with a facile

hydrothermal method, respectively. The size and shape control of α-Fe_2O_3 hollow structures from nanotubes to nanorings were achieved by simple adjustments of the reaction time and phosphate ions concentrations. The main purpose of this work is to investigate and discuss how structural aspects, such as particle size and shape of nanoparticles as well as carbon matrix, influence the electrochemical properties of the α-Fe_2O_3 nanoparticles in terms of reversible capacity, cycling performance and rate capability. The results showed that, the α-Fe_2O_3 nanotubes and α-Fe_2O_3/carbon composites exhibited the better electrochemical performance in terms of reversible capacity, capacity retention and rate performance than the other α-Fe_2O_3 hollow structures as well as cubic α-Fe_2O_3 particles, highlighting that the nanotubes with high aspect rations anchored on graphene could serve as potential anode materials for lithium-ion batteries.

2 Experimental Methods

2.1 Sample synthesis

Unless specified, all chemical regents used in this work were analytical grade and were used without further purification.

Synthesis of hollow structures α-Fe_2O_3. The hollow structures α-Fe_2O_3 was synthesized by a hydrothermal treatment of $FeCl_3$ solution in the presence of KH_2PO_4 and K_2SO_4 [17,28]. In a typical experimental procedure for α-Fe_2O_3 nanotubes, $FeCl_3 \cdot 6H_2O$ (3.78 g), KH_2PO_4 (0.052 g) and K_2SO_4 (0.070 g) aqueous solutions were mixed together, and then distilled water was then added to a final volume of 700 ml. After stirring for 10 minutes, the mixture was transferred into Teflon lined stainless steel autoclaves for hydrothermal treatment at 200 ℃, and maintained at this temperature for 48 h. The autoclaves then cooled down to room temperature naturally, and the red precipitate was separated by centrifugation, washed with distilled water and absolute ethanol, and dried under vacuum at 80 ℃. By simple adjustment of the reaction time and phosphate ions concentrations, a

series of α-Fe_2O_3 with different sizes and surface morphologies were produced.

Synthesis of α-Fe_2O_3/GNS composites. Graphene oxide (GO) used in this work was synthesized from nature graphite power by a modified Hummers method. GNS were obtained by a thermal reduction of GO. The preparation details have been described elsewhere [14]. In a typical synthesis, 0.3 g GNS and 3.125 g $FeCl_3 \cdot 6H_2O$ were dispersed in 200 ml of distilled water under ultrasonication at room temperature for 1 h. An appropriate amount of ammonia solution ($NH_3 \cdot H_2O$, 25 wt %) was added successively and the final pH of the resulting suspension was adjusted to about pH 6. Then the suspension was transferred into Teflon lined stainless steel autoclaves and maintained at 164 ℃ for 12 h. After the autoclaves cooled down to room temperature naturally, the α-Fe_2O_3/GNS composites were collected by centrifuging and washing with distilled water, followed by drying at 80 ℃ under vacuum overnight.

Synthesis of α-Fe_2O_3/CNTs composites. The α-Fe_2O_3/CNTs composites were prepared by a similar hydrothermal method with CNTs replace by GNS.

Cubic α-Fe_2O_3 particles. The cubic α-Fe_2O_3 particles were prepared accordingly by a similar hydrothermal method except for the absence of GNS or CNTs.

2.2 Sample characterization

The structures of the as-prepared materials were characterized by Cu K*a* radiation on a Bruker AXS D8 X-ray diffractometer. While, X-ray photoelectron spectroscopy (XPS) (Kratos AXIS Ultra DLD; AI (anode) X-ray source) was utilized to investigate the surface chemistries of the as-prepared materials. The composites were characterized by thermogravimetric analysis (TGA, Netzsch STA499C) under air over a temperature range of 40 ℃ to 800 ℃ with a ramp rate of 10 ℃/min. Nitrogen adsorption-desorption was determined by Brunanuer-Emmett-Teller (BET) tests using a Nova 1000e (Quantachrome Instruments) surface area and pore analyzer. Further, LEO-1530 Field

Emission Scanning Electron Microscopy (FE-SEM, Oxford Instrument) and Transmission electron microscopy (TEM, JEOL JEM-2010) were applied to observe the morphologies of the as-prepared materials.

2.3 Electrochemical measurement

The working electrodes were prepared by mixing 80 wt % active materials (α-Fe_2O_3 hollow structures, α-Fe_2O_3/GNS, α-Fe_2O_3/CNTs, and cubic α-Fe_2O_3), 10 wt % acetylene black, and 10 wt % polyvinylidene fluoride (Kynar FLEX 910, Elf Atochem, Issaquah, WA, USA) binder dissolved in N-methyl pyrrolidone (Fluka Inc., St. Louis, MO, USA) to form homogeneous slurries. The slurries were spread onto a Cu foil current collector. CR2032-type coin cells were assembled in an argon glove box for electrochemical characterization. Lithium foil was used as the negative electrode. The liquid electrolyte was 1 M $LiPF_6$ dissolved in a mixture of ethylene carbonate (EC), ethylmethyl carbonate (EMC) and dimethyl carbonate (DMC) (1:1:1 in volume %). The cells were galvanostatically charged and discharged in a battery analzyers (Neware, Shenzhen, China) for a cut-off voltage of 3.0 to 0.005 V (vs. Li/Li^+) at room-temperature. The CV and EIS measurements were performed on an electrochemical work station (CHI660D, Chenhua Ltd Co., Shanghai, China). The CV curves were measured at 0.5 mV s^{-1} over the range from 3.0 to 0.005 V. The amplitude of ac perturbation signal was 5 mV and the frequency range was varied from 10^5 to 10^{-2} Hz.

3 Results and Discussion

3.1 Characterization

The crystallographic structures of hollow structure α-Fe_2O_3 (48h), α-Fe_2O_3/GNS and α-Fe_2O_3/CNTs composites, and cubic α-Fe_2O_3 particles were analyzed by X-ray powder diffraction (XRD) in Figure 1. A few characteristic peaks for α-Fe_2O_3 (2θ=24.1, 33.2, 35.6, 64.0°), marked by their indices ((012), (104), (110), and (300)), are observed, respectively, for all of these products.

These peaks can be readily indexed to the standard hematite (PDF 33-0664). For α-Fe_2O_3/GNS composites, characteristic diffraction peak of GNS cannot be observed at 2θ of 24.5 to 27.5°, which indicates that no graphite-like layered structure is formed by re-stacking of chemically reduced graphene [22]. In case of α-Fe_2O_3/CNTs composites, a broad hump peak around 26° merged is attributed to CNTs [23,24], implying that the short-range ordered structure in the composites. These results indicate that the resultant α-Fe_2O_3 nanoparticles in the composites are pure α-Fe_2O_3 with a spinel structure.

XPS is one of the strongest techniques in characterization of materials, was employed to further reveal the valence state of elements and the chemical composition of the products. In the high-resolution Fe 2p spectrum (Figure 2(a)) for the hollow structure α-Fe_2O_3 (48 h), α-Fe_2O_3/GNS and α-Fe_2O_3/CNTs composites, two peaks at binding energies of ~711 eV for Fe 2p3/2 and ~724 eV for Fe 2p1/2 with a shake-up satellite at ~719 eV are observed, which is consistent with hematite phase [12,14]. Figure 2(b,c) show the curve fitting of C1s core levels for α-Fe_2O_3/GNS and α-Fe_2O_3/CNTs composites, respectively. The C1s XPS spectrum of both products can be fitted into three peaks, corresponding to carbon atoms in three functional groups: sp2 carbon (C-C, ~284.8 eV), carbon in C-O bonds (~286.1 eV), and carboxylate carbon (O-C=O, 288.5 eV) [25]. However, the O/C ratio in the α-Fe_2O_3/GNS composites decreases remarkably compared with that of the α-Fe_2O_3/CNTs composites, indicating that most of the oxygen-containing groups in the α-Fe_2O_3/GNS composites are successfully removed. Such a low O/C ratio of GNS implies a good electronic conductivity, which is favorable for stabilizing the electronic and ionic conductivity [26]. Thus, this obvious difference should lead to the difference of their electrochemical performance as anode materials for LIBs.

The scanning electron microscopy (SEM) images provide insight into the morphology and microstructure of the hollow structure α-Fe_2O_3 (48 h), α-Fe_2O_3/GNS and α-Fe_2O_3/CNTs composites, and cubic α-Fe_2O_3 particle. Figiure 3(a) shows the image of the hollow structure α-Fe_2O_3 without any dispersion treatment, from which it can be seen that the resultant sample exhibits nanotubes morphology with good uniformity. Figure 3(b) shows that the α-Fe_2O_3 nanoparticles are uniformly dispersed in the GNS matrix to prevent the restacking of the GNS and no large agglomeration can be found, which guarantees the good connection between α-Fe_2O_3 and GSN by plane-to-point networks and ensures the effective use of conductive GNS. Moreover, the random hybridization between α-Fe_2O_3 nanoparticles and GNS can form a three-dimensional (3D) porous structure, which is beneficial for achieving high rate performance [20]. From Figure 3(c), it can be seen that the CNTs intertwine with α-Fe_2O_3 nanoparticles whereas little agglomeration obtained, acting as branches to connect α-Fe_2O_3 nanoparticles, which can improve the electrical continuity by line-to-point contact. It can be seen from Figure 3(d) that the cubic α-Fe_2O_3 particles with lengths around 700 nm in size are obtained under similar experimental condition for preparing α-Fe_2O_3/GNS composites. TGA indicates that the amount of GNS and CNTs in the composites is about 13 wt% and 18 wt%, respectively (Figure 3(e)). The BET specific surface area of the nanotubes, short nanotubes, very short nanotubes, and nanorings is little difference, which is measured to be 11.9, 10.8, 10.0 and 9.3 $m^2\ g^{-1}$, respectively.

To provide further insight into the nanostructure of the tubes, analytical TEM investigations were also performed. Figure 4(a) shows the TEM image of the α-Fe_2O_3 nanotubes at low magnification, where the strong contrast between the dark edge and pale center further confirm the hollow clearly, namely, tubular structure. The product consists almost entirely of nanotubes with outer diameters of 130-160 nm, inner diameters of 110-130 nm. Figure 4(b) shows typical HRTEM image of a single

α-Fe_2O_3 nanotube. A lattice spacing of 0.46 nm for the (003) planes of the α-Fe_2O_3 along the nanotubes can be readily resolved, indicating the α-Fe_2O_3 nanotubes grow along the [001] direction (also the long axes of the nanotubes). The above results illustrate that the α-Fe_2O_3 nanotubes have been successfully fabricated by a double anion-assisted hydrothermal method.

3.2 Morphology and Growth Mechanism of Hematite Hollow Structures

To have a clear understanding of the growth process of the α-Fe_2O_3 nanotubes, the products under different reaction times were collected for TEM investigation, as shown in Figure 5. It can be seen that the α-Fe_2O_3 nanotubes undergo an evolution from spindlelike precursors to nanotubes. The products obtained after 3h (Figure 5(a)) show spindlelike precursors with a diameter of 160 to 250 nm and a length of 360-600 nm, as has been extensively observed in forced hydrolysis processes [23,24,27]. Prolonging the reaction time to 12h (Figure 5(b)), the size of the products did not change so much. However, there are hollow structures in some products. A mixture of semitubular and tubular structure was formed after longer reaction time (24h, Figure 5(c)). For reaction times of 48 h (Figure 4(a)), the final structure consists predominantly of nanotubes that are completely hollow.

Based on evidence from the above time-dependent morphology evolution evidence, the formation process of the nanotubes can be proposed as taking place by “dissolution” of the spindle-like precursors from the tips toward the interior along the axis resulting in semitubular and eventually hollow nanotubes [28]. Under acidic conditions (pH=2) at a 200 ℃, the sharp tips of the spindle-like precursors are highly reactive, which are easily attacked by the protons. It is clearly found that a higher proportion of the α-Fe_2O_3 nanotubes would be formed if prolonging the reaction time, and the dissolution process is not uniform resulting in partial dissolution, and the non-uniform dissolution varied from spindle to spindle and even for a single spindle.

The growth control of α-Fe_2O_3 nanocrystals by the adsorption of phosphate and sulfate ions has

been extensively studied [17,29,30]. It is proposed that the sharp tips of the spindle-like precursors may begin to dissolve in the following manner:

$$\alpha\text{-}Fe_2O_3 + 6H^+ \rightarrow 2Fe^{3+} + 3H_2O \quad (1)$$

In the process of the hydrothermal reaction, phosphate and sulfate ions can speed up the dissolution by their coordination effect with ferric ions [17].

On the basis of the time-dependent experimental results discussed above, it is reasonable to postulate that the size and surface architecture of the nanostructures could be tuned by varying the phosphate/sulfate ratio, which controls the formation of the precursors and the subsequent dissolution process. As shown in Figure 6(a-f), it is obvious that with the decrease in the amount of phosphate ions, the aspect ratio of the products decreases, and the morphology changes from tube to ring, demonstrating that the phosphate ions are responsible for the growth of the precursors, which consequently determines the sizes and aspect rations of the final hollow nanostructures. In addition, the XRD patterns of the hollow nanomaterials are shown in Figure 6(g), which match the XRD spectrum of the standard hematite (PDF 33-0664).

3.3 Electrochemical Performance.

Figure 7 shows the CV curves of α-Fe_2O_3 nanotubes, α-Fe_2O_3/GNS and α-Fe_2O_3/CNTs, and cubic α-Fe_2O_3 electrodes for the first four cycles at ambient temperature at a slow scan rate of 0.5 mV s^{-1}, respectively. As shown in Figure 7(a,b), two reduction peaks are observed in the first cathodic scan for the α-Fe_2O_3 nanotubes and α-Fe_2O_3/GNS electrode, respectively. The weak peak appears at about 1.5 V for the α-Fe_2O_3 nanotubes electrode and 1.6 V for the α-Fe_2O_3/GNS electrode, indicating that initial lithium insertion into the α-Fe_2O_3, which can be attributed to the reaction of α-Fe_2O_3 + xLi $\rightarrow$ α-$Li_xFe_2O_3$ [8,31,32]. However, there is no corresponding weak peak in the CV curves of α-Fe_2O_3/CNTs and cubic α-Fe_2O_3 electrodes, the difference among the CV curves of the α-Fe_2O_3

nanotubes, α-Fe_2O_3/GNS, α-Fe_2O_3/CNTs and cubic α-Fe_2O_3 electrodes is possible due to their different Li-ion insertion efficiency caused by the dimensions and structure characteristics. The second strong peak at about 0.5 V with a shoulder at about 0.75 V, which could be ascribed to the conversion reaction α-$Li_xFe_2O_3 + (6-x)Li \rightarrow 2Fe + 3Li_2O$ and the irreversible reaction related to the decomposition of the electrolyte [8,31,33]. The first anodic curves for the α-Fe_2O_3 nanotubes, α-Fe_2O_3/GNS and α-Fe_2O_3/CNTs, and cubic α-Fe_2O_3 electrodes are similar and include a broad peak at about 1.8 V, corresponding to the reversible oxidation of Fe^0 to Fe^{3+}. The CV curves of α-Fe_2O_3 nanotubes, α-Fe_2O_3/GNS and α-Fe_2O_3/CNTs electrodes are stable and show good reversibility after the first cycle. In the case of cubic α-Fe_2O_3 electrode (Figure 7(d)), the peak cathodic and anodic current is gradually decreased, indicating the in-sufficient oxidation-reduction reaction process during cycles. Furthermore, it is also worth noting that the CV curves of cubic α-Fe_2O_3 electrode are not well overlap, showing that the capacities could gradually decrease with increasing cycle number.

Figure 8 shows the charge/discharge curves of α-Fe_2O_3 nanotubes, α-Fe_2O_3/GNS and α-Fe_2O_3/CNTs, and cubic α-Fe_2O_3 electrodes at 0.1 C (1C =1007 mAh g^{-1}) in voltage window of 0.005-3.0 V, and these are typical charge/discharge curves for transition metal anode materials. In the discharge curve of the first cycle, there are potential slopes located at 1.2-0.9 V and an obvious potential plateau at 0.9 -0.8 V for α-Fe_2O_3 nanotubes, α-Fe_2O_3/GNS and α-Fe_2O_3/CNTs electrodes, in accordance to the reaction processes of the α-Fe_2O_3 and the electrolyte with lithium, respectively. Nevertheless, there is only a broad potential at 0.8-0.7 V for cubic α-Fe_2O_3 electrode. For the subsequent cycle, all the discharge curves show a higher voltage plateau at about 1.0-0.9 V, and the total discharge capacities are reduced. The initial discharge capacities are 1906, 2065, 2018, and 1603 mAh g^{-1} for α-Fe_2O_3 nanotubes, α-Fe_2O_3/GNS and α-Fe_2O_3/CNTs, and cubic α-Fe_2O_3 electrodes, respectively. The phenomenon that overfull capacity has been widely reported for

transition metal oxides, which is usually ascribed to the formation of the solid electrolyte interphase (SEI) film and possibly lithium consumption via interfacial reactions during the first discharge process [10]. In the subsequently cycles, the discharge capacities of α-Fe_2O_3 nanotubes, α-Fe_2O_3/GNS and α-Fe_2O_3/CNTs electrodes decrease slightly, however, the discharge capacities of cubic α-Fe_2O_3 electrodes decrease markedly.

Figure 9(a) presents the cycling performances of the α-Fe_2O_3 hollow structures, α-Fe_2O_3/GNS and α-Fe_2O_3/CNTs, and cubic α-Fe_2O_3 electrodes at 0.1 C. The rapid fading of cubic α-Fe_2O_3 electrode may result from the poor kinetics of electrochemical conversion reaction. It is obvious that α-Fe_2O_3 nanotubes electrode has the best cycling performance among the hollow structures, and the cycling performance of hollow structure α-Fe_2O_3 improves with the increase of aspect rations, which may be probably due to the nanotubes can provide more void spaces to buffer volume change and accommodate the strain associated with the volume variation, and superior electrochemical kinetics [34.35]. In addition, even naorings show a better cycling performance than that of cubic α-Fe_2O_3 electrodes. The above results demonstrate the hollow structure especially aspect rations is crucial to improve the cycling performance of α-Fe_2O_3 electrodes. After 60 cycles, the reversible capacities of the α-Fe_2O_3 nanotubes, α-Fe_2O_3/GNS and α-Fe_2O_3/CNTs, and cubic α-Fe_2O_3 electrodes are 1090, 1091, 929 and 576 mAh g^{-1}, respectively. The initial coulombic efficiencies of nanotubes, short nanotubes and very short nanotubes, and nanorings electrodes are 67.8%, 72.7%, 65.6% and 64.5%, respectively, which is higher than those of α-Fe_2O_3/GNS and α-Fe_2O_3/CNTs, and cubic α-Fe_2O_3 electrodes (Figure 9(b,c)). Figure 10 shows the durability of the α-Fe_2O_3 nanotubes, α-Fe_2O_3/GNS and α-Fe_2O_3/CNTs, and cubic α-Fe_2O_3 electrodes at a constant high rate of 5 C after an activation process at 1 C, respectively. The charge capacities of the α-Fe_2O_3 nanotubes, α-Fe_2O_3/GNS and α-Fe_2O_3/CNTs, and cubic α-Fe_2O_3 electrodes are 462, 471, 301, and 32 mAh g^{-1} after 180 cycles,

respectively, indicating that the cycling performance of nanotubes electrode is comparable to that of the α-Fe_2O_3/GNS electrode and better than that of α-Fe_2O_3/CNTs electrode as well as cubic α-Fe_2O_3 electrode. Moreover, one interesting phenomenon is that the nanotubes and short nanotubes electrodes exhibit an increasing trend of the capacity after certain cycles, similar to previous reports on other transition-MO, which is possibly attributed to the gradual activation processed during charge/discharge cycles [36].

Rate capacity is another important aspect of the development of current generation batteries. To test the cell capability, the rate capacities of the α-Fe_2O_3 hollow structures, α-Fe_2O_3/GNS and α-Fe_2O_3/CNTs, and cubic α-Fe_2O_3 electrodes, were evaluated at various rates between 0.4 and 1.0 C (Figure 11). From Figure 11(a), it is obvious that the nanotubes exhibit best rate cyclability compared to the short-nanotubes, very short-nanotubes, and nanorings. The reversible capacity of nanotubes electrode is 759.5 mAh g^{-1} at 400 mA g^{-1}, 596.3 mAh g^{-1} at 700 mA g^{-1}, 480.3 mAh g^{-1} at 1000 mA g^{-1}, respectively. When the current density reduces to 700 and 400 mA g^{-1}, the reversible capacity returns to 532.2 and 619.2 mAh g^{-1}, respectively. In contrast, The reversible capacity of α-Fe_2O_3/GNS electrode is 871.6 mAh g^{-1} at 400 mA g^{-1}, 675.0 mAh g^{-1} at 700 mA g^{-1}, 589.6 mAh g^{-1} at 1000 mA g^{-1} (Figure 11(b)), respectively, and when the current density reduces to 700 and 400 mA g^{-1}, the reversible capacity returns to 678.6 and 794.4 mAh g^{-1}, respectively, which is also comparable to that of nanotubes electrode and shows better rate cyclability than those of α-Fe_2O_3/CNTs, and cubic α-Fe_2O_3 electrodes. Thus, it is reasonable to deduce that the hybrid materials of α-Fe_2O_3 naonotubes with high aspect rations anchored on conducting graphene would be potential anode materials for high performance LIBs, and synthesis and characterization of the hybrid materials is now carrying out in our research group.

Figure 12 shows the Nyquist plots of the ac impedance for the α-Fe_2O_3 nanotubes, α-Fe_2O_3/GNS

and α-Fe_2O_3/CNTs, and cubic α-Fe_2O_3 electrodes, which were measured in the open circuit voltage state using fresh cells. The plots are similar to each other in shapes, with a semicircle appearing in the high to moderate frequency region and a straight line in the low frequency region. The inclined line in the low frequency represents the Warburg impedance, which is related to the diffusion of lithium ions in the active anode material, and the depressed semicircle in the high to moderate frequency region is ascribed to the SEI film resistance (R_s) and charge transfer resistance (R_{ct}) [37-40]. It is obvious that the size of the semicircles for the α-Fe_2O_3 nanotubes and α-Fe_2O_3/CNTs electrodes are smaller than that for cubic α-Fe_2O_3 electrode, indicating a lower $R_{(s+ct)}$, suggesting that the $R_{(s+ct)}$ is some suppressed. It is worth noticing that the size of the semicircle for α-Fe_2O_3/GNS electrode is the smallest of all, showing that the $R_{(s+ct)}$ for α-Fe_2O_3/GNS electrode is the lowest one among the α-Fe_2O_3 nanotubes, α-Fe_2O_3/CNTs and cubic α-Fe_2O_3 electrodes. Therefore, these results prove that the incorporation of GNS is benefit to Li^+ transport and the interleaved electron transfer high-way built up by GNS, thus leading to the enhanced electrode reaction kinetics and better electrochemical performance during charge/discharge process.

4 Conclusions

In summary, α-Fe_2O_3 hollow structures from nanotubes to nanorings, α-Fe_2O_3/GNS and α-Fe_2O_3/CNTs composites, and cubic α-Fe_2O_3 particles were successfully synthesized via a self-assemble combined with a facile hydrothermal method, respectively. By properly adjustments of the reaction time and phosphate ions concentrations, size and shape control of the α-Fe_2O_3 hollow structures are achieved. Electrochemical measurements show that the cycling performance of hollow structure α-Fe_2O_3 improves with the increase of aspect rations, namely, the α-Fe_2O_3 nanotubes exhibited the best reversible lithium storage capacities, rate capability and cycling performance, which is comparable to that of α-Fe_2O_3 nanoparticles-carbon composites. The results suggest that the

flexibility and adaptability of the self-assembly route could be utilized to prepare a variety of hybrid materials of α-Fe_2O_3 naonotubes with high aspect rations anchored on conducting graphene, and could serve as a general strategy for developing high-performance anode for lithium-ion batteries.

Acknowledgment

The authors acknowledge financial supports by the Fundamental Research Funds for the Central Universities (2013XK07).

Reference

[1] H. B. Geng, Q. Zhou, Y. Pan, H. W. Gu and J. W. Zheng, *Nanoscale*, 2014, **6**, 3889.

[2] M. Y. Son, Y. J. Hong, J. K. Lee and Y. C. Kang, *Nanoscale*, 2013, **5**, 11592.

[3] K. T. Park, F. Xia, S. W. Kim, S. B. Kim, T. Song, U. Paik and W. Il. Park, *J. Phys. Chem. C*, 2013, **117**, 1037.

[4] J. H. Kim and Y. C. Kang, *Nanoscale*, 2014, **6**, 4789.

[5] X. Zhang, Y. T. Qian, Y. C. Zhu and K. B. Tang, *Nanoscale*, 2014, **6**, 1725.

[6] P. S. Veluri and S. Mitra, *RSC Adv.*, 2013, **3**, 15132.

[7] L. Chen, H. Y. Xu, L. Li, F. F. Wu, J. Yang and Y. T. Qian, *J. Power Sources*, 2014, **245**, 429.

[8] S. Chaudhari and M. Srinivasan, *J. Mater. Chem.*, 2012, **22**, 23049.

[9] Y. Q. Zou, J. Kan and Y. Wang, *J. Phys. Chem. C*, 2011, **115**, 20747.

[10] J. M. Ma, J. B. Lian, X. C. Duan, X. D. Liu and W. J. Zheng, *J. Phys. Chem. C*, 2010, **114**, 10671.

[11] B. Wang, J. S. Chen, H. B. Wu, Z. Y. Wang and X. W. Lou. *J. Am. Chem. Soc.*, 2011, **133**, 17146.

[12] X. L. Hu, J. C. Yu and J. M. Gong, *J. Phys. Chem. C*, 2007, **111**, 11180.

[13] H. M. Fan, G. J. You, Y. Li, Z. Zheng, H. R. Tan, Z. X. Shen, S. H. Tang and Y. P. Feng, *J. Phys. Chem. C*, 2009, **113**, 9928.

[14] Z. G. An, J. J. Zhang, S. L. Pan and F. Yu, *J. Phys. Chem. C*, 2009, **113**, 8092.

[15] B. Y. Xia, Y. Yan, X. Wang and X. W. Lou, *Mater. Horiz.*, 2014, **1**, 379.

[16] Z. Y. Wang, L. Zhou and X. W. Lou, *Adv. Mater.*, 2012, **24**, 1903.

[17] C. J. Jia, L. D. Sun, F. Luo, X. D. Han, L. J. Heyderman, Z. G. Yan, C. H. Yan, K. Zheng, Z. Zhang, M. Takano, N. Hayashi, M. Eltschka, M. Klaui, U. Rudiger, T. Kasama, L.

Cervera-Gontard, R. E. Dunin-Borkowski, G. Tzvetkov and J. Raabe, *J. Am. Chem. Soc*., 2008, **130**, 16968.

[18] S. L. Chou, J. Z. Wang, D. Wexler, K. Konstantinov, C. Zhong, H. K. Liu and S. X. Dou, *J. Mater. Chem*., 2010, **20**, 2092.

[19] C. Wu, H. Zhang, Y. X. Wu, Q. C. Zhuang, L. L. Tian and X. X. Zhang, *Electrochim. Acta*, 2014, **134**, 18.

[20] L. L. Tian, Q. C. Zhuang, J. Li, C. Wu, Y. L. Shi and S. G. Sun, *Electrochim. Acta*, 2012, **65**, 153.

[21] C. Wu, Q. C. Zhuang, L. L. Tian, Y. L. Cui and X. X. Zhang, *Mater. Lett*., 2013, **107**, 27.

[22] D. Z. Chen, H. Y. Quan, J. F. Liang and L. Guo, *Nanoscale*, 2013, **5**, 9684.

[23] Y. Q. Zou, J. Kan and Y. Wang, *J. Phys. Chem. C*, 2011, **115**, 20747.

[24] T. Sugimoto, A. Muramatsu, K. Sakata and D. J. Shindo, *J. Colloid Interface Sci.*, 1993, **158**, 420.

[25] N. J. Reeves and S. Mann, *J. Chem. Soc., Faraday Trans*., 1991, **87**, 3875.

[26] X. H. Ma, X. Y. Feng, C. Song, B. K. Zou, C. X. Ding, Y. Yu, and C. H. Chen, *Electrochim. Acta*, 2013, **93**, 131.

[27] S. Bai, S. Q. Chen, X. P. Shen, G. X. Zhu and G. X. Wang, *RSC Adv.*, 2012, **2**, 10977.

[28] C. J. Jia, L. D. Sun, Z. G. Yan, L. P. You, F. Luo, X. D. Han, Y. C. Pang, Z. Zhang and C. H. Yan, *Angew. Chem. Int. Ed.*, 2005, **44**, 4328.

[29] W. Wu, X. H. Xiao, S. F. Zhang, J. Zhou, L. X. Fan, F. Ren and C. Z. Jiang, *J. Phys. Chem. C*, 2010, **114**, 16092.

[30/] L. L. Li, Y. Chu, Y. Liu and L. H. Dong, *J. Phys. Chem. C*, 2007, **111**, 2123.

[31] Z. Y. Cao and B. Q. Wei, *J. Power Sources*, 2013, **241**, 330.

[32] X. Wang, W. Tian, D. Q. Liu, C. Y. Zhi, Y. Bando and D. Golberg, *Nano Energy*, 2013, **2**, 257.

[33] S. Q. Chen, P. Bao and G. X. Wang, *Nano Eergy*, 2013, **2**, 425.

[34] H. Xiao, Y. Xia, W. K. Zhang, H. Huang, Y. P. Gan and X. Y. Tao, *J. Mater. Chem. A*, 2013, **1**, 2307

[35] R. G. Ma, M. Wang, D. T. Dam, Y. C. Dong, Y. Chen, S. K. Moon, Y. J. Yoon, J. M. Lee, *ChemPlusChem*, DOI: 10.1002/cplu.201402236

[36] A. P. Hu, X. H. Chen, Y. H. Tang, Q. L. Tang, L.Yang and S. P. Zhang, *Electrochem. Commun*., 2013, **28**, 139.

[37] M. V. Reddy, T. Yu, C. H. Sow, Z. X. Shen, C. T. Lim, G. V. Subba Rao and B. V. R. Chowdari, *Adv. Funct. Mater.*, 2007, **17**, 2792.

[38] J. X. Li, Y. Zhao, Y. H. Ding and L. H. Guan, *RSC Adv.*, 2012, **2**, 4205.

[39] D. Z. Chen, W. Wei, R. N. Wang, J. C. Zhu and L. Guo, *New J. Chem.*, 2012, **36**, 1589.

[40] S. Y. Liu, J. Xie, Q. Pan, C. Y. Wu, G. S. Cao, T. J. Zhu and X. B. Zhao, *Int. J. Electrochem. Sci.*, 2012, **7**, 354.

Figure Captions:

Figure 1. XRD pattern of α-Fe_2O_3 hollow structure (48h), α-Fe_2O_3/GNS and α-Fe_2O_3/CNTs composites, and cubic α-Fe_2O_3 particles.

Figure 2. (a) XPS survey spectrum of the α-Fe_2O_3 hollow structure (48h), α-Fe_2O_3/GNS and α-Fe_2O_3/CNTs composites, C1s high-resolution XPS spectra of (b) α-Fe_2O_3/GNS and (c) α-Fe_2O_3/CNTs composites, and their fitting results.

Figure 3. SEM images of (a) hollow structure (48h), (b) α-Fe_2O_3/GNS and (c) α-Fe_2O_3/CNTs composites, (d) cubic α-Fe_2O_3 particles, (e) TGA curves of α-Fe_2O_3/GNS and α-Fe_2O_3/CNTs composites.

Figure 4. (a, b) TEM of nanotubes under different magnifications, (c) HRTEM image.

Figure 5. TEM of the α-Fe_2O_3 hollow structures obtained after (a) 6 h, (b) 12 h, (c) 24 h.

Figure 6. SEM and TEM images of the three hollow structures: (a, b) short nanotubes, (c, d) very short nanotubes, (e, f) nanorings; (g) XRD patterns of the α-Fe_2O_3 hollow structures.

Figure 7. CV curves of (a) nanotubes, (b) α-Fe_2O_3/GNS and (c) α-Fe_2O_3/CNTs composites, (d) cubic α-Fe_2O_3 electrodes from the first to the fourth cycle at a scan rate of 0.5 mV s^{-1} in the potential range of 0.005-3.0 V (versus Li/Li^+).

Figure 8. The charge-discharge curves of (a) nanotubes, (b) α-Fe_2O_3/GNS and (c) α-Fe_2O_3/CNTs composites, (d) cubic α-Fe_2O_3 electrodes between 0.005 and 3.0 V at 0.1 C.

Figure 9. Cycling performance of the α-Fe_2O_3 hollow structures, α-Fe_2O_3/GNS and α-Fe_2O_3/CNTs composites, and cubic α-Fe_2O_3 electrodes at 100 mA g^{-1}, (b) coulombic efficiencies of the hollow structures electrodes, (c) coulombic efficiencies of α-Fe_2O_3/GNS and α-Fe_2O_3/CNTs composites, and cubic α-Fe_2O_3 electrodes.

Figure 10. Cycling performance of nanotubes, α-Fe_2O_3/GNS and α-Fe_2O_3/CNTs composites, and

cubic α-Fe_2O_3 electrodes at 5 C, respectively.

Figure 11. (a) Rate capability of nanotubes, short nanotubes, very short nanotubes, and nanorings , (b) Rate capability of α-Fe_2O_3/GNS and α-Fe_2O_3/CNTs composites, and cubic α-Fe_2O_3 electrodes at various rates between 400 and 1000 mA g^{-1}.

Figure 12. Impedance plots for electrodes containing nanotubes, α-Fe_2O_3/GNS and α-Fe_2O_3/CNTs composites, and cubic α-Fe_2O_3 particles. The frequency range applied is 100 KHz-0.01 Hz.

Figure 1

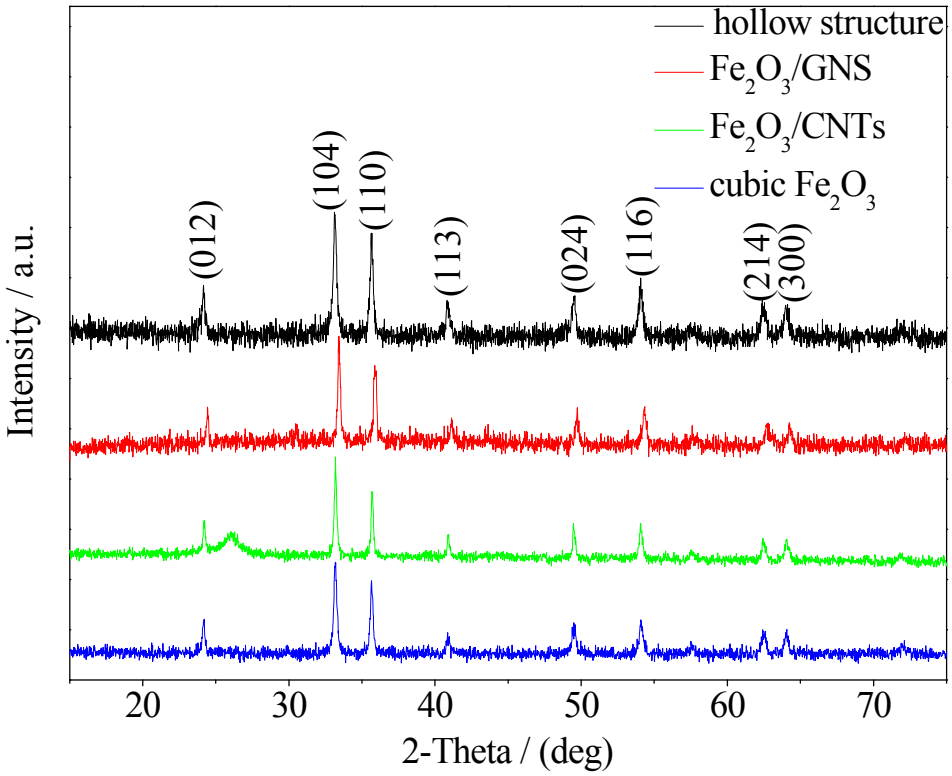

Figure 2

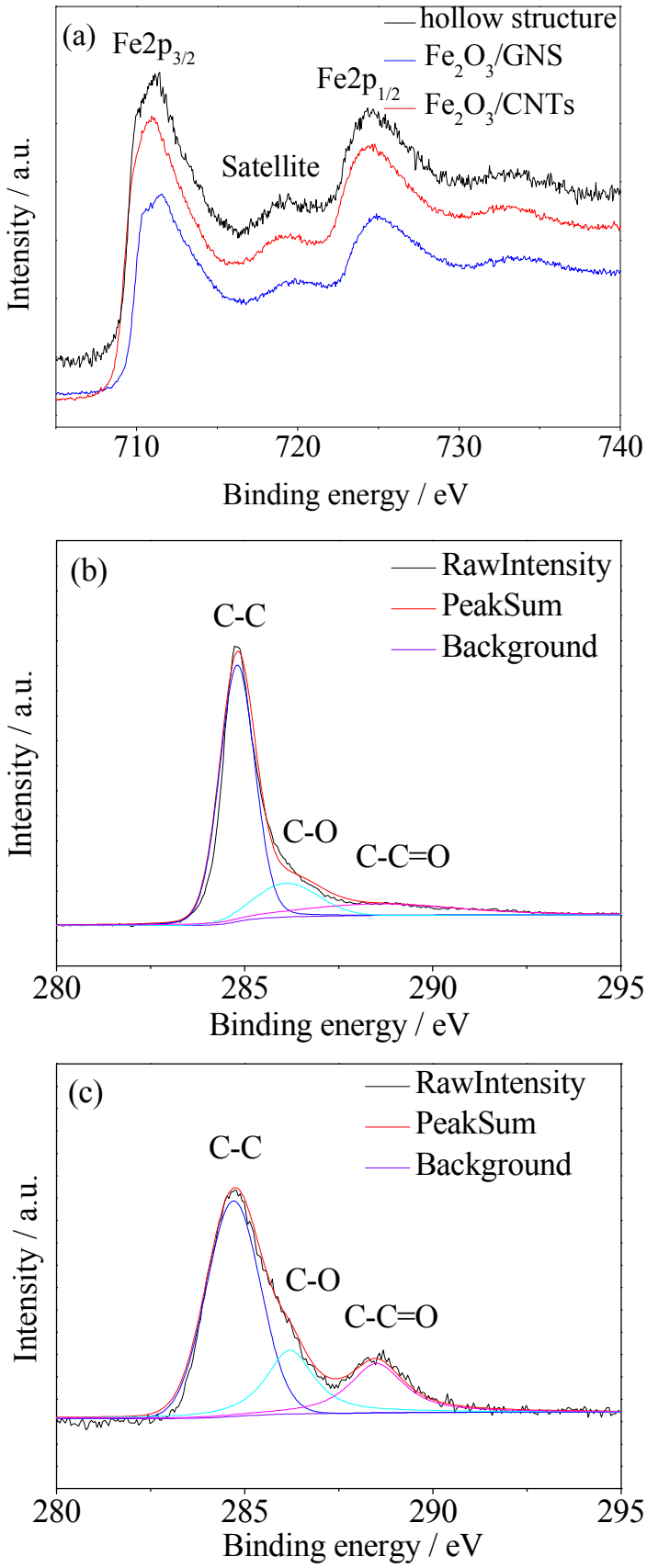

Figure 3

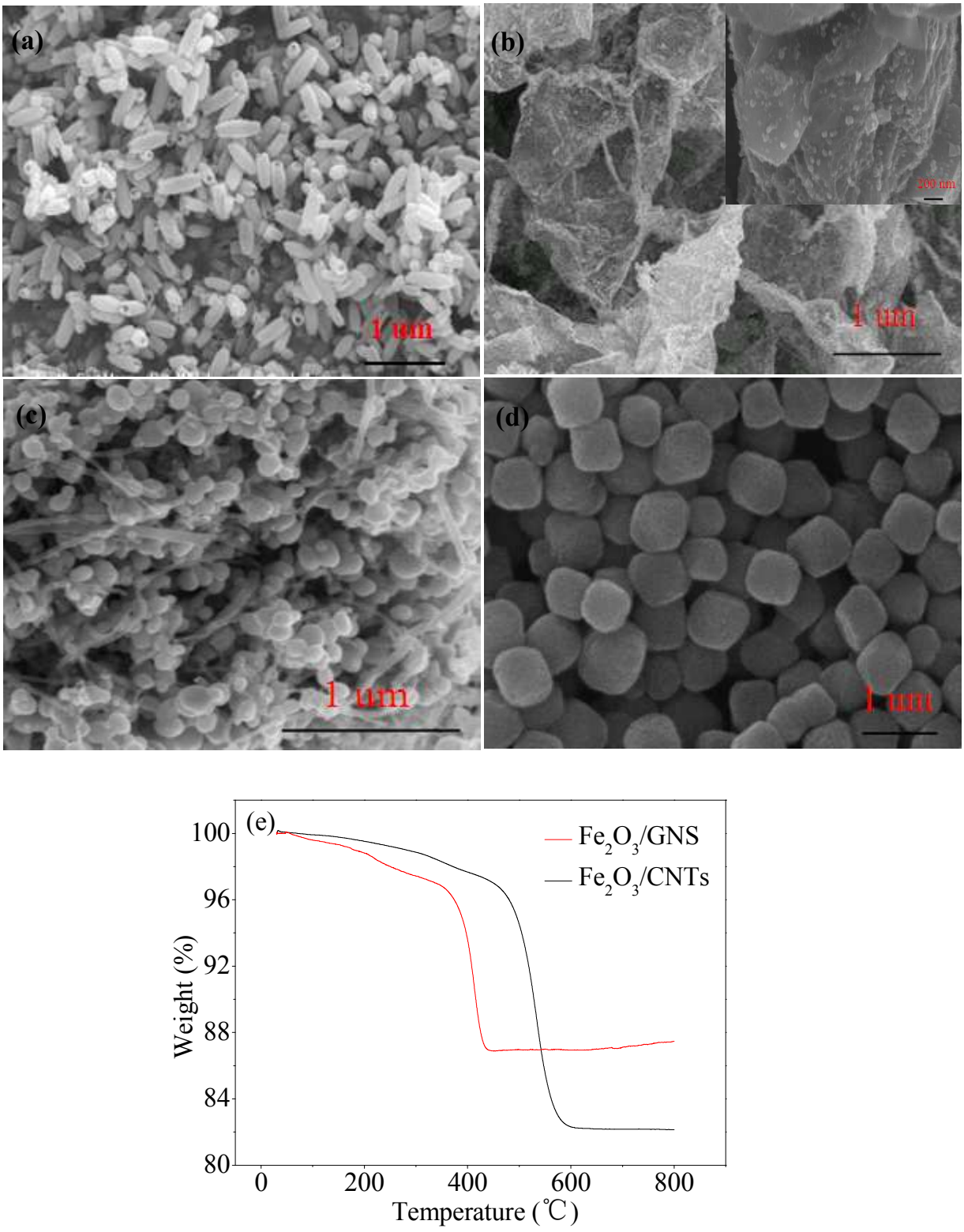

Figure 4

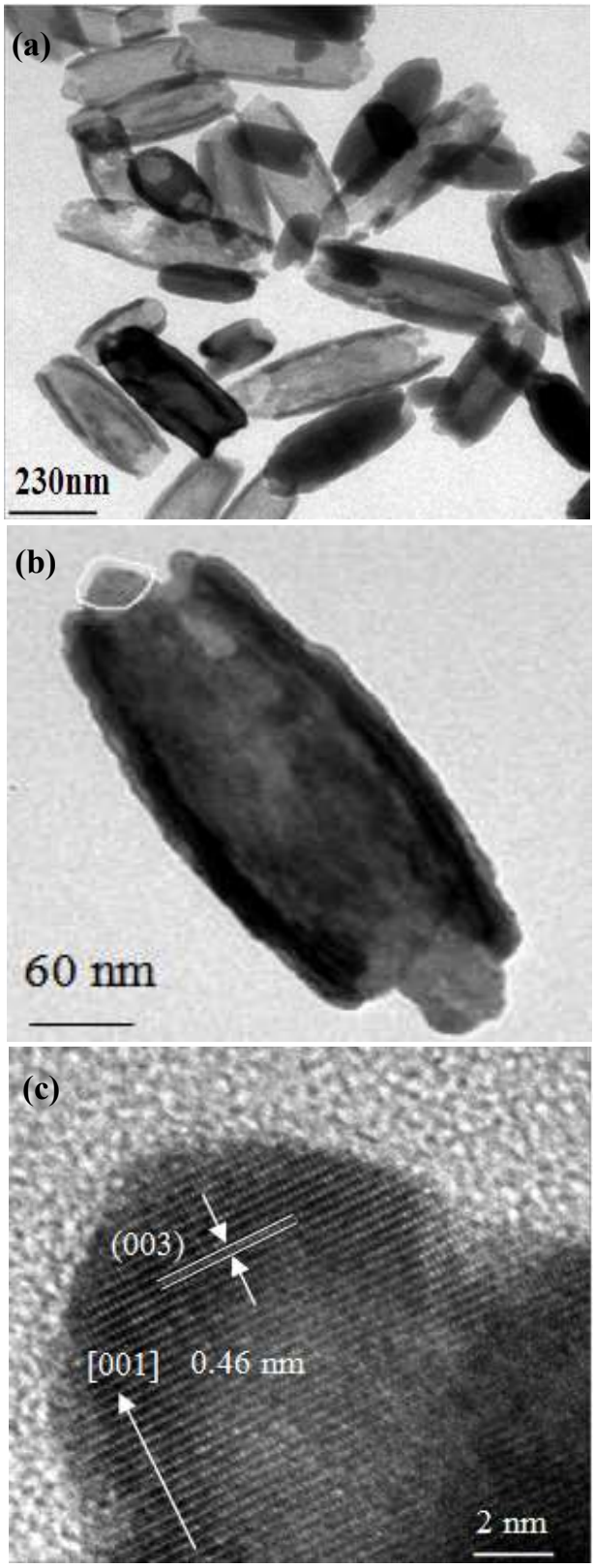

Figure 5

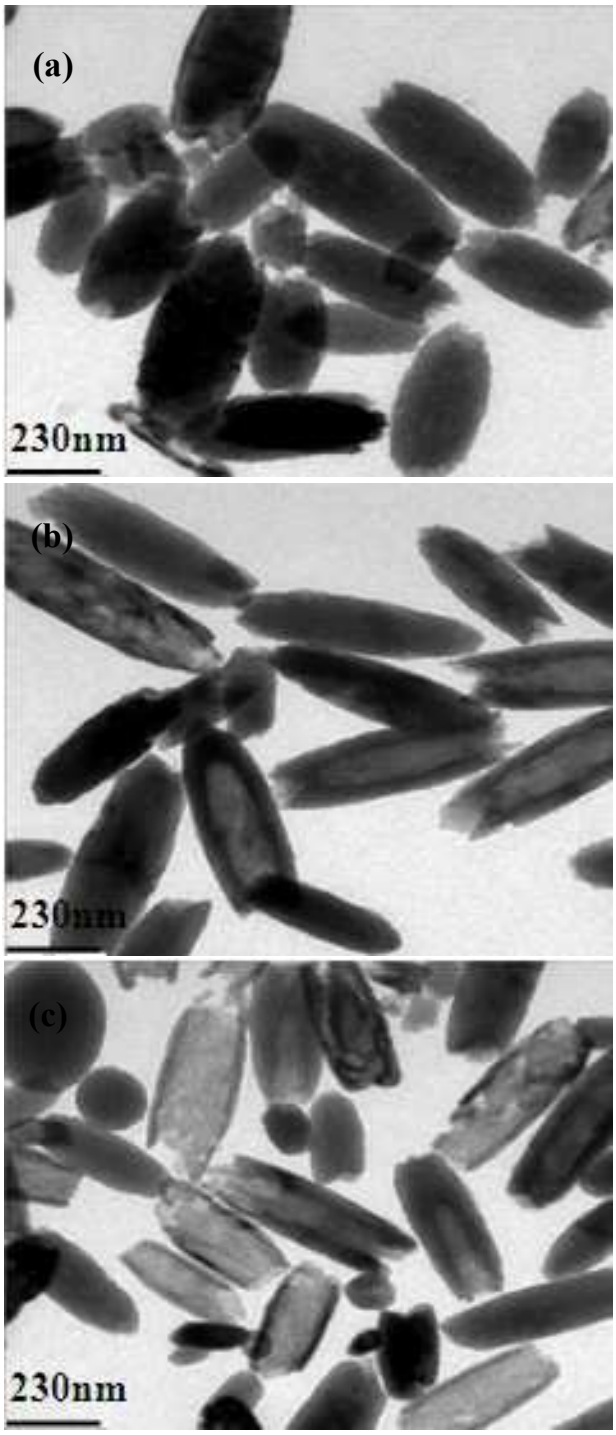

Figure 6

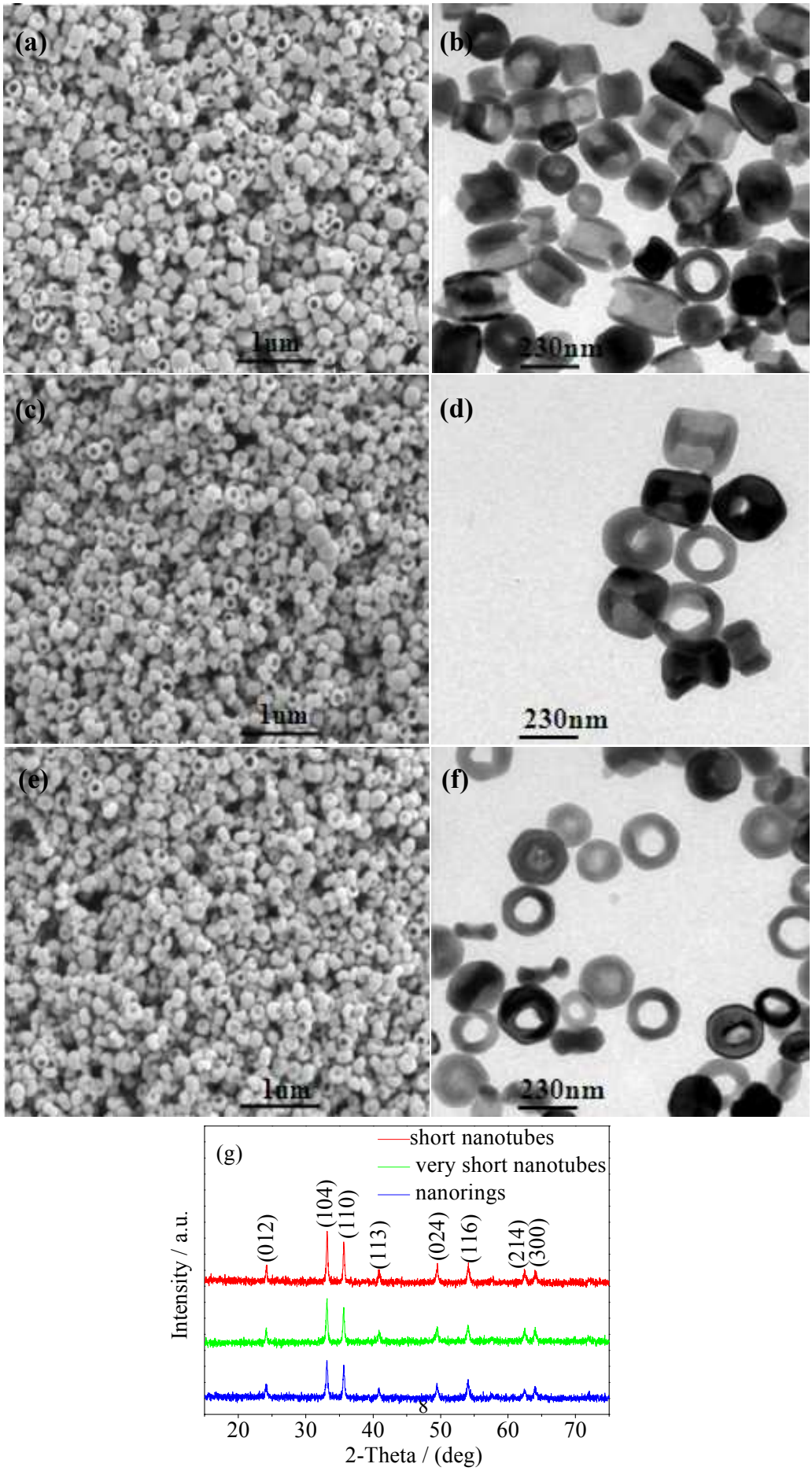

Figure 7

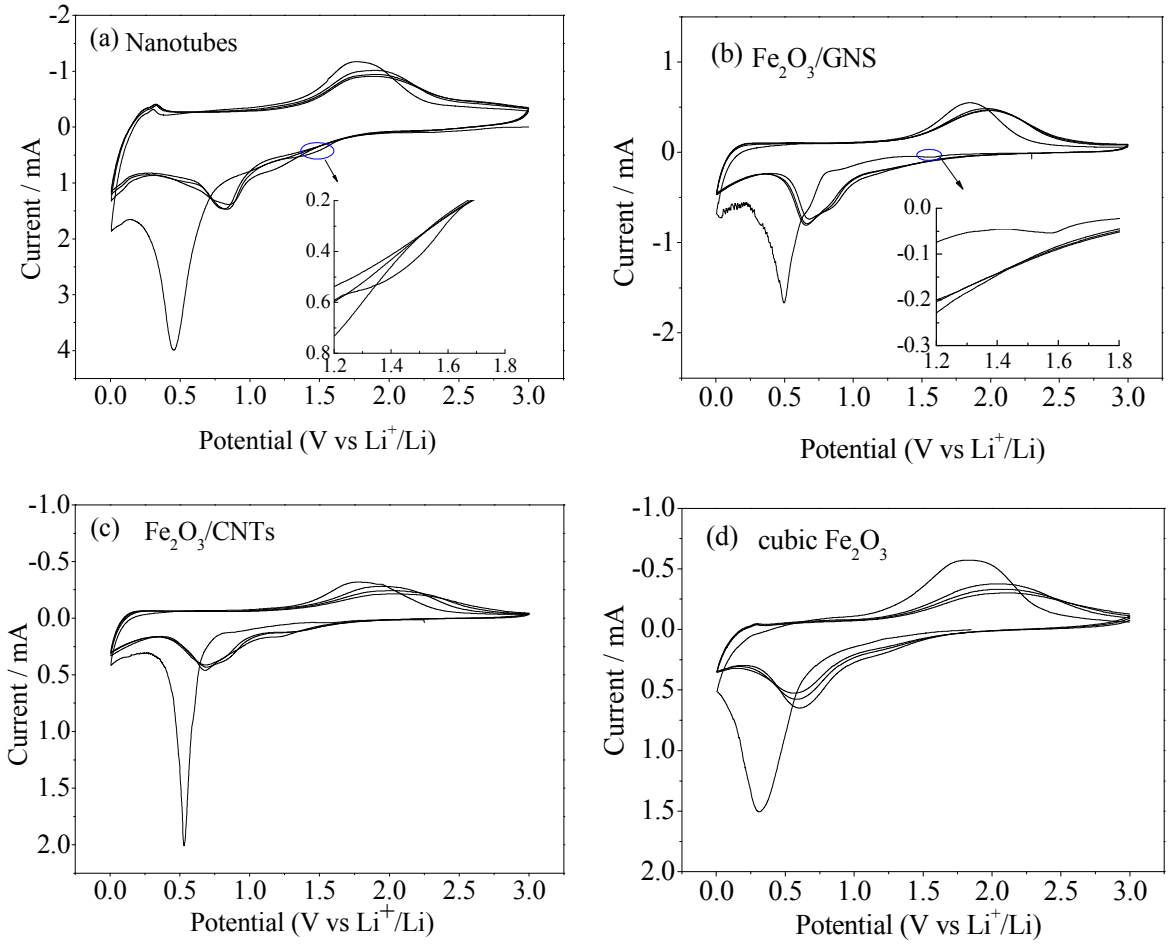

Figure 8

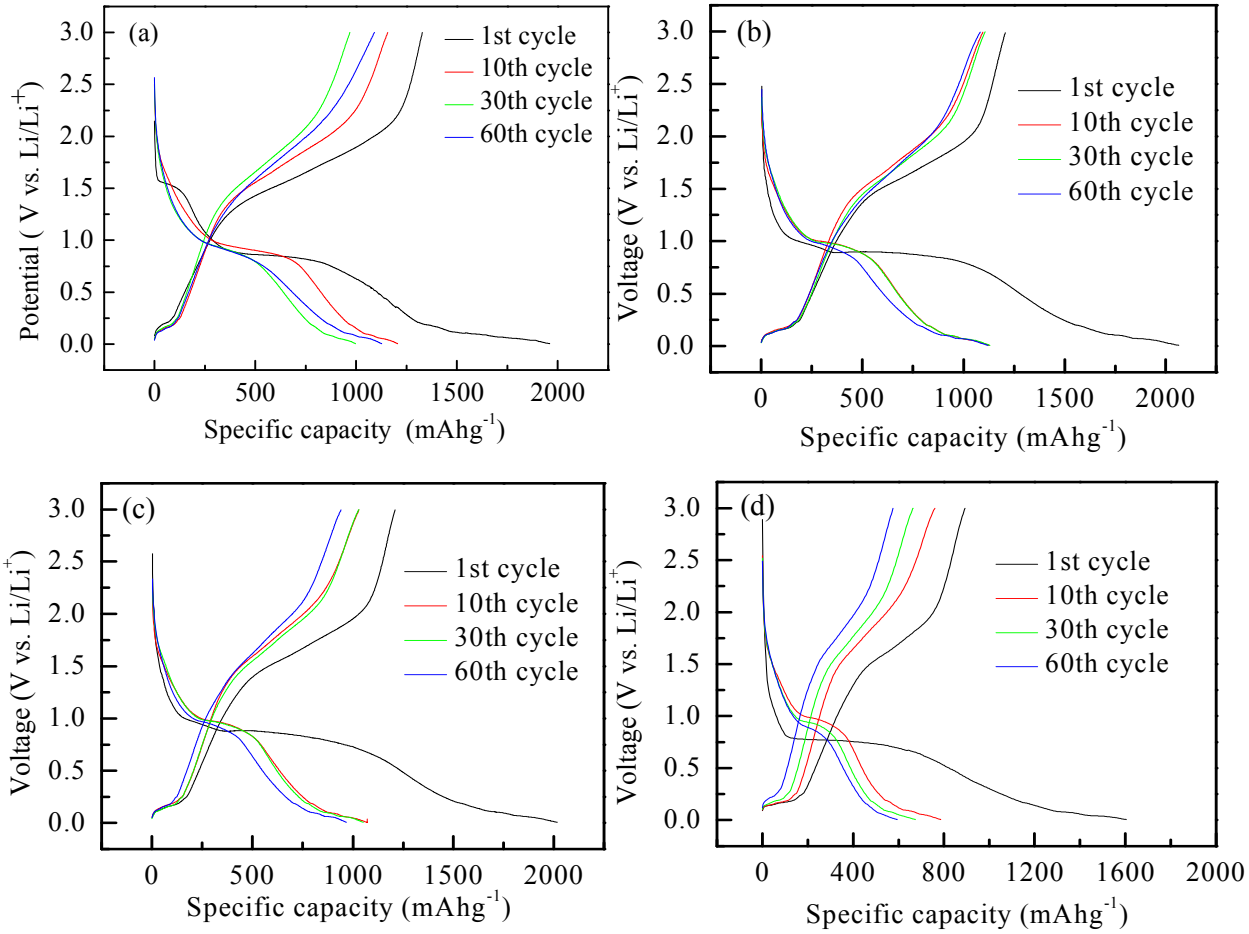

Figure 9

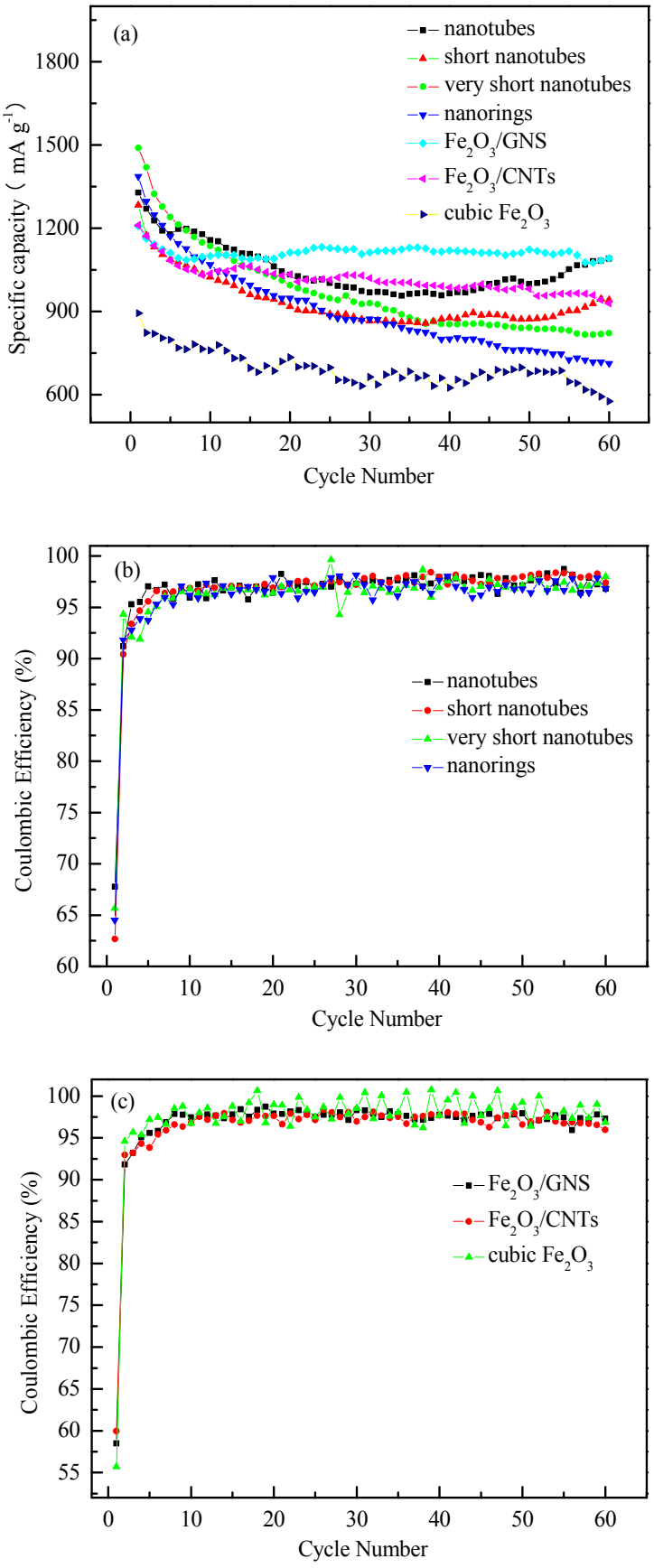

Figure 10

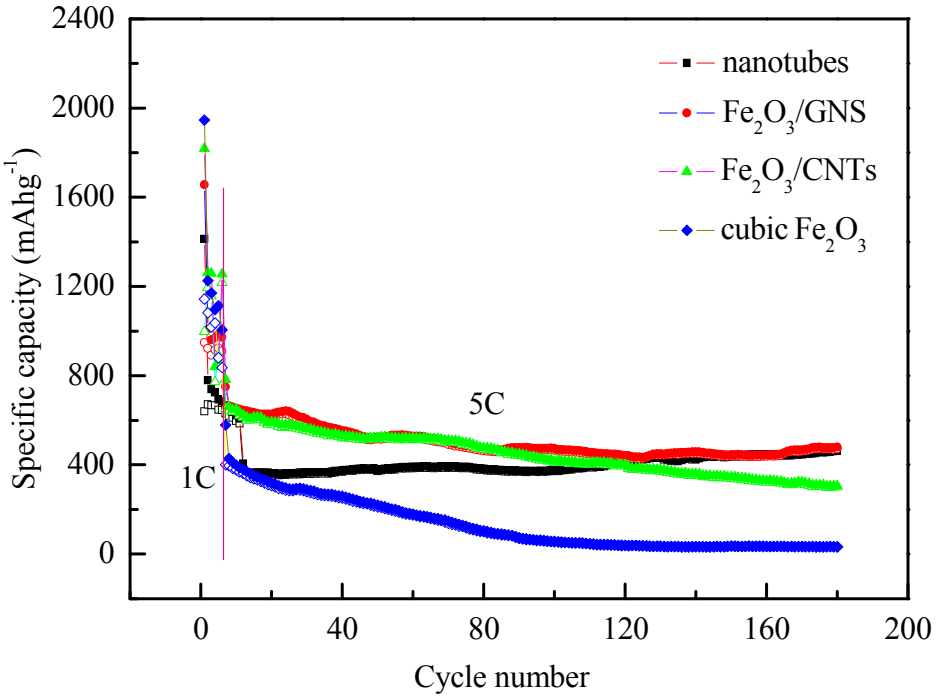

Figure 11

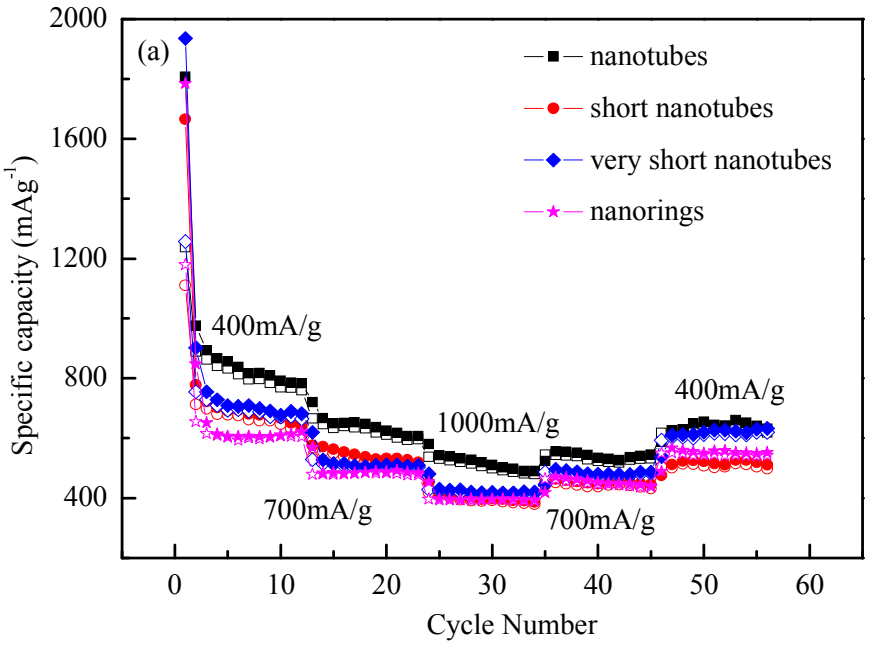

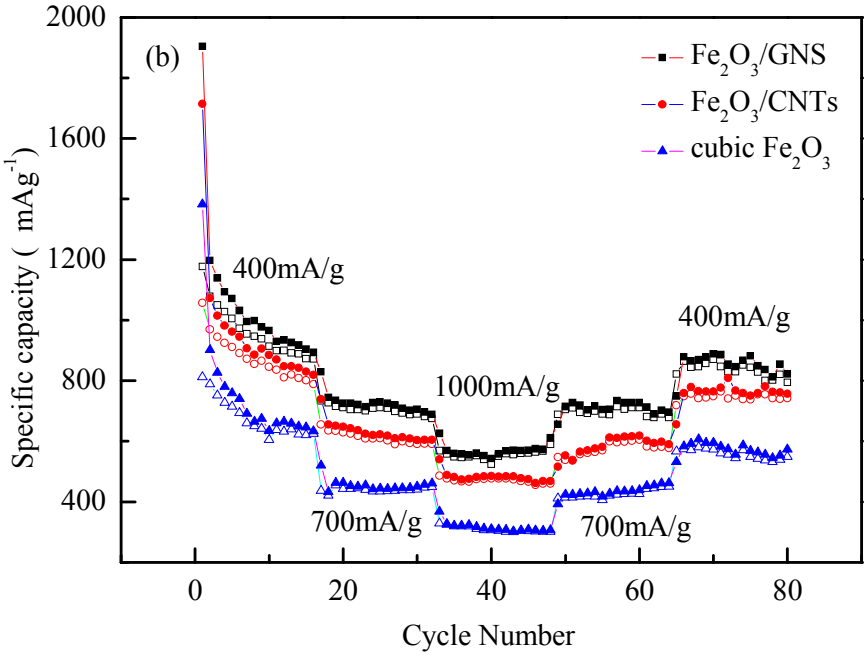

Figure 12